

TOPOLOGICAL MATTER

Experimental observation of Weyl points

Ling Lu,^{1*} Zhiyu Wang,² Dexin Ye,² Lixin Ran,² Liang Fu,¹
John D. Joannopoulos,¹ Marin Soljačić¹

The massless solutions to the Dirac equation are described by the so-called Weyl Hamiltonian. The Weyl equation requires a particle to have linear dispersion in all three dimensions while being doubly degenerate at a single momentum point. These Weyl points are topological monopoles of quantized Berry flux exhibiting numerous unusual properties. We performed angle-resolved microwave transmission measurements through a double-gyroid photonic crystal with inversion-breaking where Weyl points have been theoretically predicted to occur. The excited bulk states show two linear dispersion bands touching at four isolated points in the three-dimensional Brillouin zone, indicating the observation of Weyl points. This work paves the way to a variety of photonic topological phenomena in three dimensions.

In 1929, Hermann Weyl derived (1) the massless solutions to the Dirac equation—the relativistic wave equation for electrons. Neutrinos were thought, for decades, to be Weyl fermions until the discovery of the neutrino mass. Moreover, it has been suggested that low-energy excitations in condensed matter (2–12) can be the solutions to the Weyl Hamiltonian $H(\mathbf{k}) = v_x k_x \sigma_x + v_y k_y \sigma_y + v_z k_z \sigma_z$, where v_i and k_i are the group velocities and momenta and σ_i are the Pauli matrices. Recently, photons have also been proposed to emerge as Weyl particles inside photonic crystals (13). In all cases, two linear dispersion bands in three-dimensional (3D) momentum space intersect at a single degenerate point—the Weyl point. Weyl points are 3D extensions of the 2D Dirac cones, as in graphene, possessing unique density of states and transport properties (14). Notably, Weyl points are monopoles of Berry flux with topological charges defined by the Chern numbers (4, 5). These topological invariants enable materials containing Weyl points to exhibit a variety of unusual phenomena, including topological surface states (15), chiral anomaly (16), quantum anomalous Hall effect (17), and others (18, 19). Furthermore, Weyl points are the intermediate topological gapless phases between topologically distinct bandgap materials (20), facilitating the search for other topological phases in 3D. In this work, we report on the observation of Weyl points in an inversion-breaking 3D double-gyroid (DG) photonic crystal without breaking time-reversal symmetry.

Weyl points are sources of quantized Berry flux in the momentum space (see the supplementary text). Their charges can be defined by the corresponding Chern numbers of ± 1 (Fig. 1A). So, Weyl points robustly appear in pairs

and can only be removed through pair annihilation. Because the Berry curvature is strictly zero under \mathcal{PT} symmetry—the product of parity (\mathcal{P} , inversion) and time-reversal symmetry (\mathcal{T})—isolated Weyl points only exist when at least one of \mathcal{P} or \mathcal{T} is broken. In (13), frequency-isolated Weyl points were predicted in \mathcal{PT} -breaking DG photonic crystals. In our experiment, we chose to break \mathcal{P} instead of \mathcal{T} to avoid using lossy magnetic materials and external magnetic fields. This choice also allows our approach to be directly extended to photonic crystals at optical wavelengths.

In Fig. 1B, we plotted the body-centered-cubic (bcc) Brillouin zone (BZ) of the \mathcal{P} -breaking DG shown in Fig. 1C. When \mathcal{T} is preserved, there must exist even pairs of Weyl points (13). The two pairs of Weyl points illustrated in the (101) plane of the BZ, in Fig. 1B, are thus the minimum number of Weyl points possible. The band structure plotted in Fig. 1D shows two linear band crossings along $\Gamma - N$ and $\Gamma - H$; the other two Weyl points have identical dispersions due to \mathcal{T} . The four Weyl points are isolated in frequency and well separated in the momentum space, making their characterization easier.

We work at the microwave frequencies around 10 GHz, where fabrication of 3D photonic crystals is more accessible. Additive processes such as 3D printing cannot yet fulfill the material requirement of having low-loss dielectrics with high-dielectric constants. To fabricate two interpenetrating gyroids with a subtractive fabrication process, we open up each gyroid network by layers along the [101] direction with equal thickness of $a/\sqrt{2}$. Here, a is the cubic lattice constant. The cylindrical defects are introduced in each layer of the red gyroid in Fig. 1C.

We approximate each gyroid network by three sets of hole drillings, as illustrated in Fig. 2A. Similar methods of drilling and angled etching have been used in the fabrication of 3D photonic crystals in the microwave (21) and near-infrared wavelengths (22). The three cylindrical air holes

of the blue gyroid, along x , y , and z , go through $(0,1/4,0)a$, $(0,0,1/4)a$, and $(1/4,0,0)a$, respectively. All air holes have a diameter of $0.54a$. Gyroids approximated by this drilling approach have almost identical band structures as those defined by the level-set isosurfaces in (13).

The second (red) gyroid is the inversion counterpart of the blue gyroid. To break \mathcal{P} , we shrink the red gyroid at $(1/4, -1/8, 1/2)a$ to be a cylinder oriented along [101]. Shown in Fig. 2B, the defect cylinder has a diameter of $0.1a$ and height of $0.2a$. We separate the red gyroid by cutting (101) planes at the centers of the defect cylinders. The blue gyroid, without introduced defects, is separated at the corresponding position of $(-1/4, 1/8, -1/2)a$. Each layer is $a/\sqrt{2}$ thick. The separated layers of each gyroid are identical up to translations of \mathbf{a}_2 (the bcc lattice vector in Fig. 1C). One unit vertical period of DG consists of two layers from each gyroid (Fig. 2B).

The materials of choice are slabs of ceramic-filled plastics (C-STOCK AK, Cuming Microwave Corp., MA) of dielectric constant 16 and loss tangent 0.01. Each slab has a thickness of 9.5 mm ($= a/\sqrt{2}$). Both the width and the length of the slabs are 304 mm (~ 12 inches). The material hardness is adjusted between 80 and 90 on a Shore D gauge to be machined by carbide tools without cracking. Each layer experienced around 700 drillings along $\pm 45^\circ$ away from its surface normal (in x and z) and about 40 ball-end millings in-plane (in y) on both top and bottom surfaces. These operations were performed using a computer-numerical-controlled three-axis vertical milling machine (fig. S1A). Although all slabs of the same gyroid can in principle be machined together, we processed no more than two layers at the same time to leave a solid frame for handling. About 20 mm were left undrilled from each of the four edges of the slabs. We subsequently cut two sides of the frames of each gyroid for their assembly (fig. S1B). Figure 2B illustrates that the layers of the two gyroids were offset vertically by half of the slab thickness (4.25 mm). A picture of the assembled sample is shown in Fig. 2C (more pictures are in fig. S1, C and D). The final sample in measurements consists of a total of 20 layers, with 10 layers from each gyroid stacked in alternating order (23).

We performed angle-resolved transmission measurements on the photonic crystal sample to probe the dispersions of the 3D bulk states (24–26). The schematic of the experimental setup is shown in Fig. 3A (also see fig. S1E). A pair of lens antennas were placed on the two sides of the sample. Transmission amplitudes (S -parameter S_{21}) were recorded by the network analyzer. The half-power beam widths (divergent angles) of the lens antennas were 9° . The collimated beam impinged on the sample (101) surface, in which the incident angle is varied by rotating the sample around the vertical axis. As illustrated in Fig. 3B, the component of the incident wave vector parallel to the sample surface [$k_0 \sin(\theta)$] is conserved up to a reciprocal lattice vector of the sample surface, due to the discrete

¹Department of Physics, Massachusetts Institute of Technology (MIT), Cambridge, MA 02139, USA. ²Laboratory of Applied Research on Electromagnetics (ARE), Zhejiang University, Hangzhou, Zhejiang 310027, China.
*Corresponding author. E-mail: linglu@mit.edu

Fig. 1. Weyl points in the BZ of a \mathcal{P} -breaking gyroid photonic crystal.

(A) Weyl points are monopoles of Berry flux in the momentum space. (B) The BZ of the DG photonic crystal in (C). The (101) surfaces are highlighted in green. Four Weyl points are

illustrated on the green (101) plane along $\Gamma - H$ and $\Gamma - N$, where $H = (0,1,0)2\pi/a$ and $N = (-1/2,0,1/2)2\pi/a$.

(C) The bcc cell of the DG with a \mathcal{P} -breaking cylindrical defect on the red gyroid, where $\mathbf{a}_1 = (-1,1,1)a/2$, $\mathbf{a}_2 = (1,-1,1)a/2$, and $\mathbf{a}_3 = (1,1,-1)a/2$. (D) The photon dispersions are plotted along $N - \Gamma - H$. The Weyl points are the linear band touchings between the fourth and fifth bands.

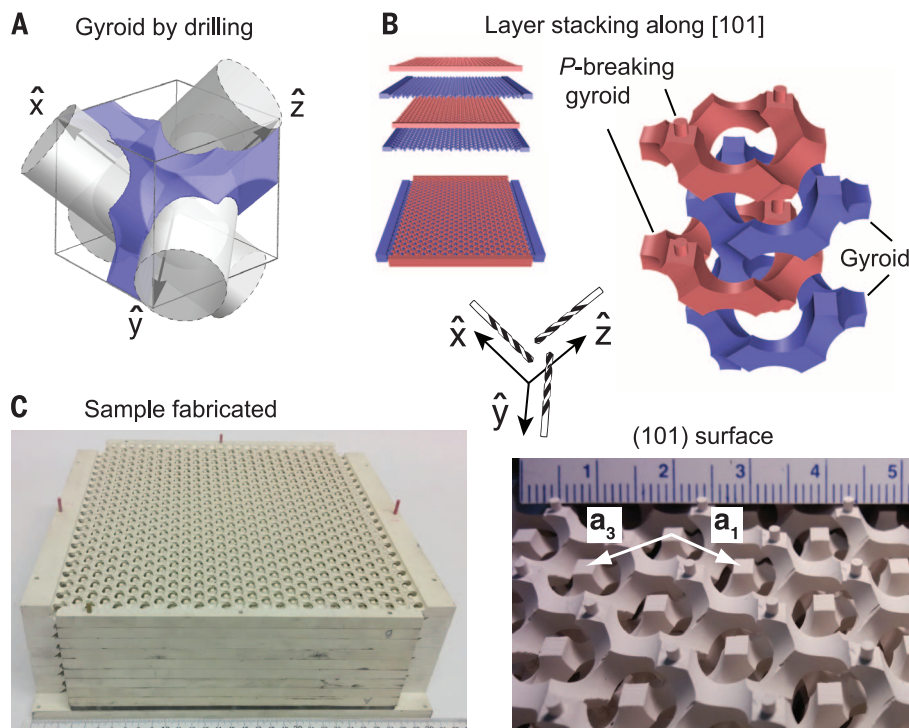
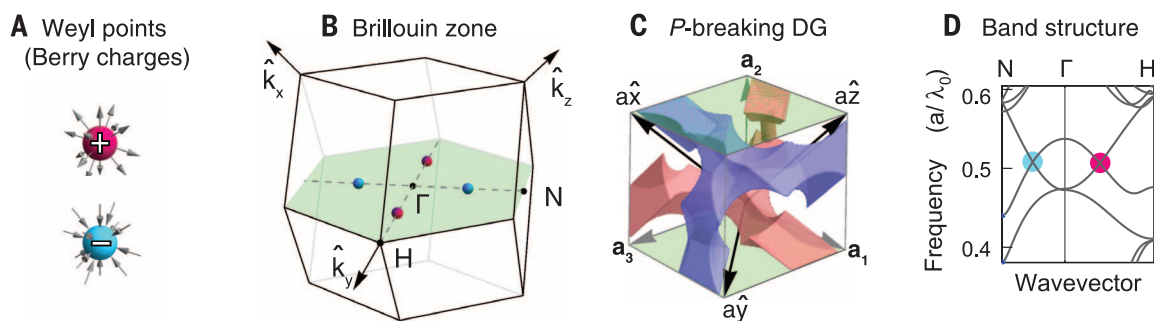


Fig. 2. Fabrication of gyroids by drilling and stacking layers. (A) Illustration in a bcc unit cell that a single gyroid structure can be approximated by drilling periodic air holes along the x , y , and z directions. (B) The DG structure can be made by stacking layers along the $[101]$ direction. The red and blue gyroids, being inversion counterparts, interpenetrate each other. We shrink the vertical connections of the red gyroid to thin cylinders in order to break \mathcal{P} . (C) (Left) A total of 20 layers were stacked. (Right) A zoom-in view from the top, with a ruler (in centimeters) in the background.

translational symmetry. All the bulk states of the same wave-vector projection (dashed line in Fig. 3B) and frequency could be excited in the bulk and exit the sample in the same direction as the incident beam. The exiting signal was collected by the antenna at the opposite side. A pair of prisms was used to increase the magnitudes of the incident wave vectors for sampling a larger volume in the BZ. We placed the angled prisms (12.4°) in contact with the opposite surfaces of the sample (Fig. 3A); the prisms are made of the same material as the sample ($\epsilon = 16$).

Both the source and receiving antennas were linearly polarized. To account for the complex polarization response in the 3D \mathcal{P} -breaking photonic crystal, we summed up the transmitted power of different polarizations to resolve more bulk states in the sample. Illustrated in Fig. 3A, the electric-field directions of the s and p polarizations are vertical and parallel to the incident plane, respectively. We first set the source antenna to be in one of the polarization states (e.g., s) and measured the transmitted power twice by setting the receiving antenna to be s and p polarized, respectively. The sum of the two trans-

mitted signals was normalized to the transmission signal without the sample. Second, we set the source antenna to be the other polarization (e.g., p) and repeated the above procedure. Last, we summed the transmission power for both polarizations and plotted it in Fig. 3C. For details, see figs. S2 and S3.

We mapped out all 3D bulk states, projected along $[101]$, by varying θ and α as shown in Fig. 3, A and B. Six sets of transmission data of representative directions are plotted in Fig. 3C. The transmission data stop on the right slanted boundary, which corresponds to the maximum rotation angle in θ . Close to this boundary, the transmission intensity is low due to the smaller effective cross section of the samples at large angles. For comparison, the corresponding band structures (projected along the transmission direction $[101]$) are plotted as figure insets. In principle, all states in the projected band structure can be observed in the transmission data, where the transmission amplitudes are proportional to the bulk density of states. However, the coupling and transmission efficiencies depend on the details of the Bloch mode polarizations, modal symmetries, radiation lifetimes, finite size effects, group velocities, and Berry-curvature-induced anomalous velocities. Although the signal strength varies in some areas in the experimental data, all the transmission responses (Fig. 3C) compare very well and are consistent with the theoretical band structures in the insets.

When $\alpha = 90^\circ$ (in Fig. 3), the beam scans through the upper Weyl point along $\Gamma - H$, represented by a magenta sphere in Fig. 3B. The outline of the transmission intensity in Fig. 3C clearly shows a linear point crossing around 11.3 GHz in frequency and close to $0.45(2\pi/a)$ in wave vector. As α increases from 90° to 105° and 120° , we are moving off the Weyl point and observe the opening of a small gap. This gap opening is expected for a point degeneracy and excludes the possibility of the state being associated with a line degeneracy [line node (13)]. Because photons do not have spin or polarization degeneracies in our crystal, every band dispersion represents a single state, excluding the possibility of being a four-fold 3D Dirac degeneracy (27). Due to the aspect ratio of our sample, we were unable to scan the dispersions

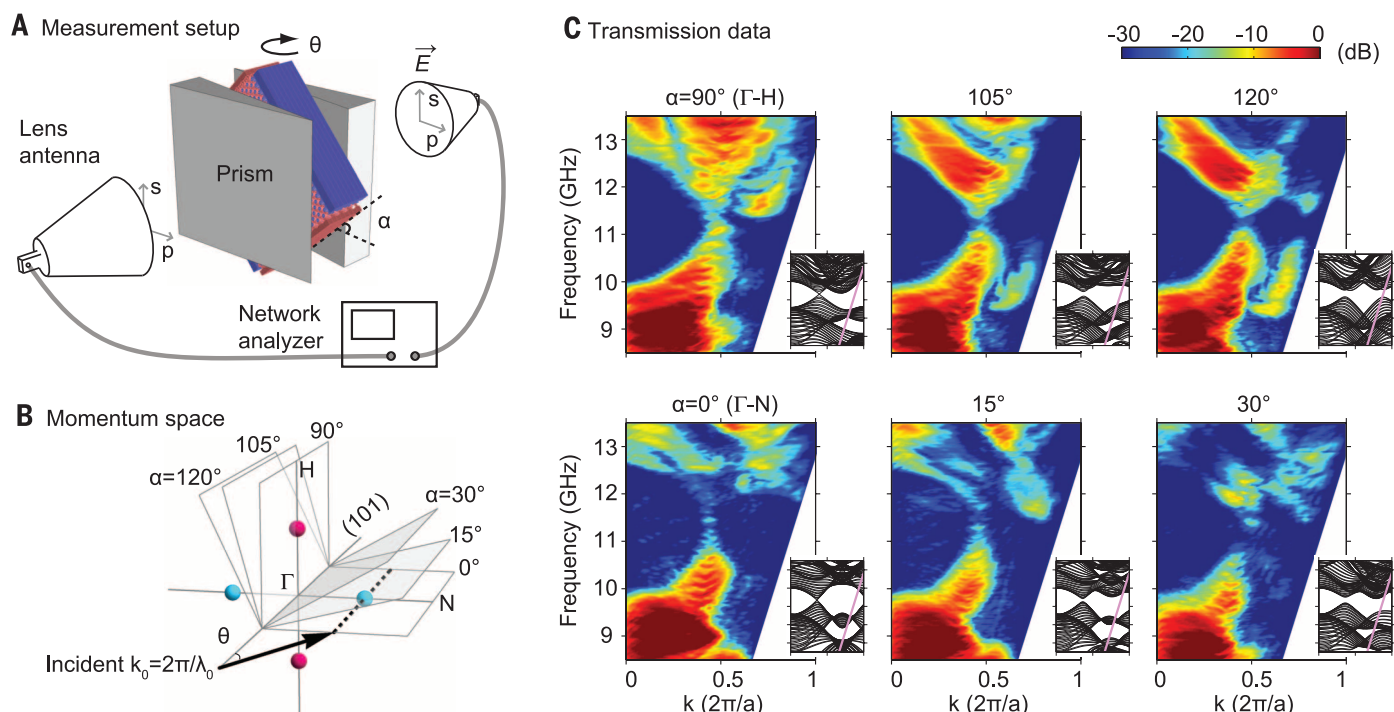


Fig. 3. Angle-resolved transmission measurements. (A) Schematic of the microwave transmission setup. (B) The bulk states of the \mathbf{k} vectors on the dashed line can be excited by the incident wave at incidence angle θ . (C) Transmission data, summed over both s and p polarizations, as the sample is rotated along the $[101]$ axis by the angle α . The insets show the calculated band structures projected along $[101]$; they are scaled to the same range and ratio as the measured data.

along the $[101]$ transmission direction. However, our transmission data do contain all the contributions from those dispersions projected together. For example, the resonance lines below and above the Weyl point, in Fig. 3C ($\alpha = 90^\circ$), indicate the gap opening along the $[101]$ direction as well. Similarly, the other Weyl point, in cyan, on the right of the $\Gamma - N$ axis, is studied by orienting α to be 0° , 15° , and 30° . Although the transmission intensity of the upper bulk bands is not as prominent, the Weyl point dispersions can still be inferred. The remaining two Weyl points, at the opposite \mathbf{k} locations, relate to the two measured Weyl points by T . They have the same projected band dispersions and the same transmission pattern as the data shown in Fig. 3C.

The photonic Weyl points observed in our experiment pave the way to topological photonics (28–31) in 3D, where 3D Dirac points (27, 32) and various gapped topological phases (33, 34) can be accessed. Similar approaches can be readily adopted to observe Weyl points at optical frequencies using 3D nanofabrication (35–37). The surface states, not seen in our transmission experiments, could potentially be characterized through reflection spectra or evanescent-wave measurements. Close to the Weyl-point frequencies, photonic Weyl materials provide angular selectivity (38) for filtering light from any 3D incident angle. The unique density of states at the Weyl point can potentially enable devices such as high-power single-mode lasers (39).

REFERENCES AND NOTES

- H. Weyl, *Z. Phys.* **56**, 330–352 (1929).
- C. Herring, *Phys. Rev.* **52**, 365–373 (1937).
- A. Abrikosov, S. Beneslavskii, *Sov. Phys. JETP* **32**, 699 (1971).
- G. E. Volovik, *The Universe in a Helium Droplet* (Oxford Univ. Press, Oxford, 2009).
- X. Wan, A. M. Turner, A. Vishwanath, S. Y. Savrasov, *Phys. Rev. B* **83**, 205101 (2011).
- A. A. Burkov, L. Balents, *Phys. Rev. Lett.* **107**, 127205 (2011).
- G. Xu, H. Weng, Z. Wang, X. Dai, Z. Fang, *Phys. Rev. Lett.* **107**, 186806 (2011).
- J. Liu, D. Vanderbilt, *Phys. Rev. B* **90**, 155316 (2014).
- D. Bulmash, C.-X. Liu, X.-L. Qi, *Phys. Rev. B* **89**, 081106 (2014).
- M. Hirayama, R. Okugawa, S. Ishibashi, S. Murakami, T. Miyake, *Phys. Rev. Lett.* **114**, 206401 (2015).
- H. Weng, C. Fang, Z. Fang, B. A. Bernevig, X. Dai, *Phys. Rev. X* **5**, 011029 (2015).
- S.-M. Huang *et al.*, *Nat. Commun.* **6**, 7373 (2015).
- L. Lu, L. Fu, J. D. Joannopoulos, M. Soljačić, *Nat. Photonics* **7**, 294–299 (2013).
- P. Hosur, S. A. Parameswaran, A. Vishwanath, *Phys. Rev. Lett.* **108**, 046602 (2012).
- A. C. Potter, I. Kimchi, A. Vishwanath, *Nat. Commun.* **5**, 5161 (2014).
- H. Nielsen, M. Ninomiya, *Phys. Lett. B* **130**, 389–396 (1983).
- K.-Y. Yang, Y.-M. Lu, Y. Ran, *Phys. Rev. B* **84**, 075129 (2011).
- A. M. Turner, A. Vishwanath, *Topological Insulators* **6**, 293–324 (2013).
- P. Hosur, X. Qi, *C. R. Phys.* **14**, 857–870 (2013).
- S. Murakami, *New J. Phys.* **9**, 356 (2007).
- E. Yablonovitch, T. J. Gmitter, K. M. Leung, *Phys. Rev. Lett.* **67**, 2295–2298 (1991).
- S. Takahashi *et al.*, *Nat. Mater.* **8**, 721–725 (2009).
- L. Lu *et al.*, *Opt. Lett.* **37**, 4726–4728 (2012).
- W. M. Robertson *et al.*, *Phys. Rev. Lett.* **68**, 2023–2026 (1992).
- E. Özbay *et al.*, *Phys. Rev. B* **50**, 1945–1948 (1994).
- C. Pouya, P. Vukusic, *Interface Focus* **2**, 645–650 (2012).
- S. M. Young *et al.*, *Phys. Rev. Lett.* **108**, 140405 (2012).
- L. Lu, J. D. Joannopoulos, M. Soljačić, *Nat. Photonics* **8**, 821–829 (2014).
- Z. Wang, Y. Chong, J. D. Joannopoulos, M. Soljačić, *Nature* **461**, 772–775 (2009).
- M. Hafezi, S. Mittal, J. Fan, A. Migdall, J. Taylor, *Nat. Photonics* **7**, 1001–1005 (2013).
- M. C. Rechtsman *et al.*, *Nature* **496**, 196–200 (2013).
- Z. K. Liu *et al.*, *Science* **343**, 864–867 (2014).
- L. Fu, *Phys. Rev. Lett.* **106**, 106802 (2011).
- L. Lu, C. Fang, S. G. Johnson, J. D. Joannopoulos, M. Soljačić, *arXiv 1507.00337* (2015).
- E. J. Crossland *et al.*, *Nano Lett.* **9**, 2807–2812 (2009).
- M. D. Turner, G. E. Schröder-Turk, M. Gu, *Opt. Express* **19**, 10001–10008 (2011).
- M. D. Turner *et al.*, *Nat. Photonics* **7**, 801–805 (2013).
- Y. Shen *et al.*, *Science* **343**, 1499–1501 (2014).
- S.-L. Chua, L. Lu, J. Bravo-Abad, J. D. Joannopoulos, M. Soljačić, *Opt. Lett.* **39**, 2072–2075 (2014).

ACKNOWLEDGMENTS

We thank A. Gallant and E. Johnson at the MIT central machine shop for machining the gyroid layers; Y. Shen, B. Zhang, J. Liu, B. Zhen, B. Wang, A. Vishwanath, H. Chen, Q. Yan, and C. Fang for discussions; and P. Rebusco for critical reading and editing of the manuscript. J.D.J. was supported in part by the U.S. Army Research Office through the Institute for Soldier Nanotechnologies under contract W911NF-13-D-0001. L.F. was supported by the U.S. Department of Energy (DOE) Office of Basic Energy Sciences, Division of Materials Sciences and Engineering, under award DE-SC0010526. L.L. was supported in part by the Materials Research Science and Engineering Center Program of the NSF under award DMR-1419807. M.S. and L.L. (analysis and reading of the manuscript) were supported in part by the MIT Solid-State Solar-Thermal Energy Conversion Center and Energy Frontier Research Center of DOE under grant DE-SC0001299. Z.W. D.Y., and L.R. were supported by the Chinese National Science Foundation (CNSF) under grants 61401395, 61401393, and 61131002, respectively.

SUPPLEMENTARY MATERIALS

www.sciencemag.org/content/349/6248/622/suppl/DC1
Supplementary Text
Figs. S1 to S3

15 February 2015; accepted 6 July 2015
Published online 16 July 2015
10.1126/science.aaa9273



Supplementary Materials for

Experimental observation of Weyl points

Ling Lu,* Zhiyu Wang, Dexin Ye, Lixin Ran,
Liang Fu, John D. Joannopoulos, Marin Soljačić

*Corresponding author. E-mail: linglu@mit.edu

Published 16 July 2015 on *Science Express*
DOI: 10.1126/science.aaa9273

This PDF file includes:

Supplementary Text
Figs. S1 to S3

Correction: Figure S1 has been updated.

Supplementary Text

Chern numbers of the Weyl points

We show the Weyl points carry a non-zero Chern number of ± 1 , using the $\mathbf{k.p}$ theory.

The Weyl hamiltonian, omitting the constant velocities, is

$$H(\mathbf{k}) = k_x \sigma_x + k_y \sigma_y + k_z \sigma_z = \begin{pmatrix} k_z & k_x - ik_y \\ kx +iky & -k_z \end{pmatrix} = k \begin{pmatrix} \cos \theta & \cos \theta e^{-i\phi} \\ \cos \theta e^{i\phi} & -\cos \theta \end{pmatrix}$$

, where $k = |\mathbf{k}|$ in the spherical coordinates.

The eigenvalues

$$E_1 = k \text{ and } E_2 = -k$$

The eigenvectors

$$\psi_1 = \begin{pmatrix} \cos \frac{\theta}{2} e^{i\phi} \\ -\sin \frac{\theta}{2} \end{pmatrix} \text{ and } \psi_2 = \begin{pmatrix} \sin \frac{\theta}{2} e^{i\phi} \\ \cos \frac{\theta}{2} \end{pmatrix}$$

Here the subscripts (1 and 2) label the two dispersion bands degenerate at the Weyl point.

The Berry connections

$$\mathcal{A}_1(\mathbf{k}) = \langle \psi_1 | i \nabla_{\mathbf{k}} | \psi_1 \rangle = \langle \psi_1 | i \left(\frac{\partial}{\partial k}, \frac{1}{k} \frac{\partial}{\partial \theta}, \frac{1}{k \sin \theta} \frac{\partial}{\partial \phi} \right) | \psi_1 \rangle = (A_r, A_\theta, A_\phi) = (0, 0, \frac{-\cot \frac{\theta}{2}}{2k})$$

$$\mathcal{A}_2(\mathbf{k}) = \langle \psi_2 | i \nabla_{\mathbf{k}} | \psi_2 \rangle = (0, 0, \frac{-\tan \frac{\theta}{2}}{2k})$$

The Berry curvatures

$$\mathcal{F}_1(\mathbf{k}) = \nabla_{\mathbf{k}} \times \mathcal{A}_1(\mathbf{k}) = (F_r, F_\theta, F_\phi) = (\frac{1}{2k^2}, 0, 0)$$

$$\mathcal{F}_2(\mathbf{k}) = \nabla_{\mathbf{k}} \times \mathcal{A}_2(\mathbf{k}) = (\frac{-1}{2k^2}, 0, 0)$$

The curvatures are pointing in the radial directions; Weyl points are Berry monopoles.

The Chern number is the surface integration of the Berry curvatures enclosing the Weyl point:

$$\int \mathcal{F}_1(\mathbf{k}) ds = k^2 \int_0^\pi \sin \theta d\theta \int_0^{2\pi} d\phi F_r(\mathbf{k}) = 2\pi \int_0^\pi d\theta [\frac{\sin \theta}{2}] = 2\pi$$

$$\int \mathcal{F}_2(\mathbf{k}) ds = -2\pi.$$

The corresponding Chern numbers are ± 1 ; they are the charges of the Weyl points. The topological invariants do not change, when the surface of integration deforms from a sphere.

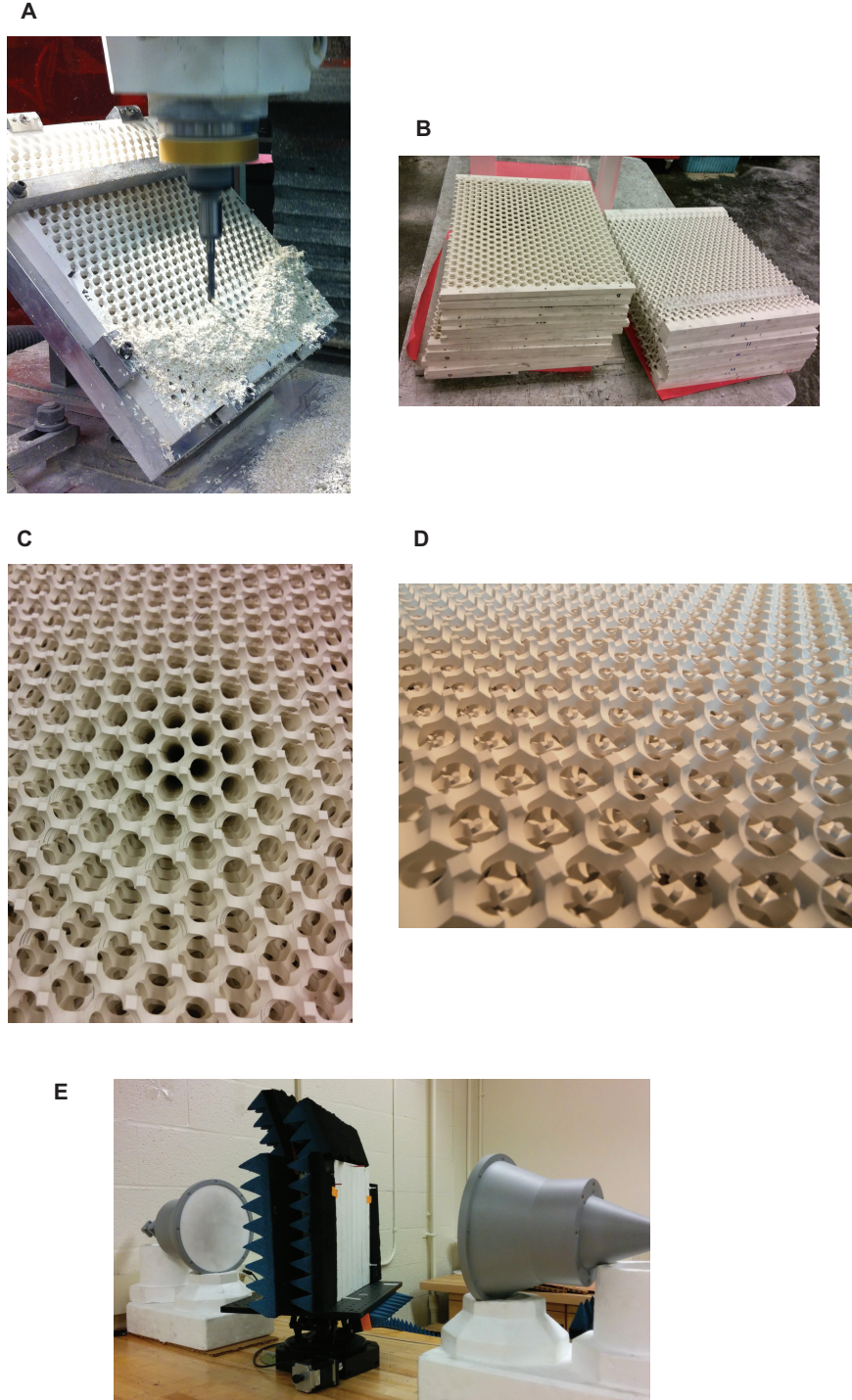


FIG. S1: Sample fabrication and measurement setup. (A) Angled drilling of the slabs on a milling machine. (B) Two piles of machined slabs of the two gyroids. (C) Stacked single-gyroid layers (without \mathcal{P} -breaking defects). (D) Stacked double-gyroid layers. (E) Image of the microwave transmission setup.

$\alpha = 90^\circ$ (Γ -H)

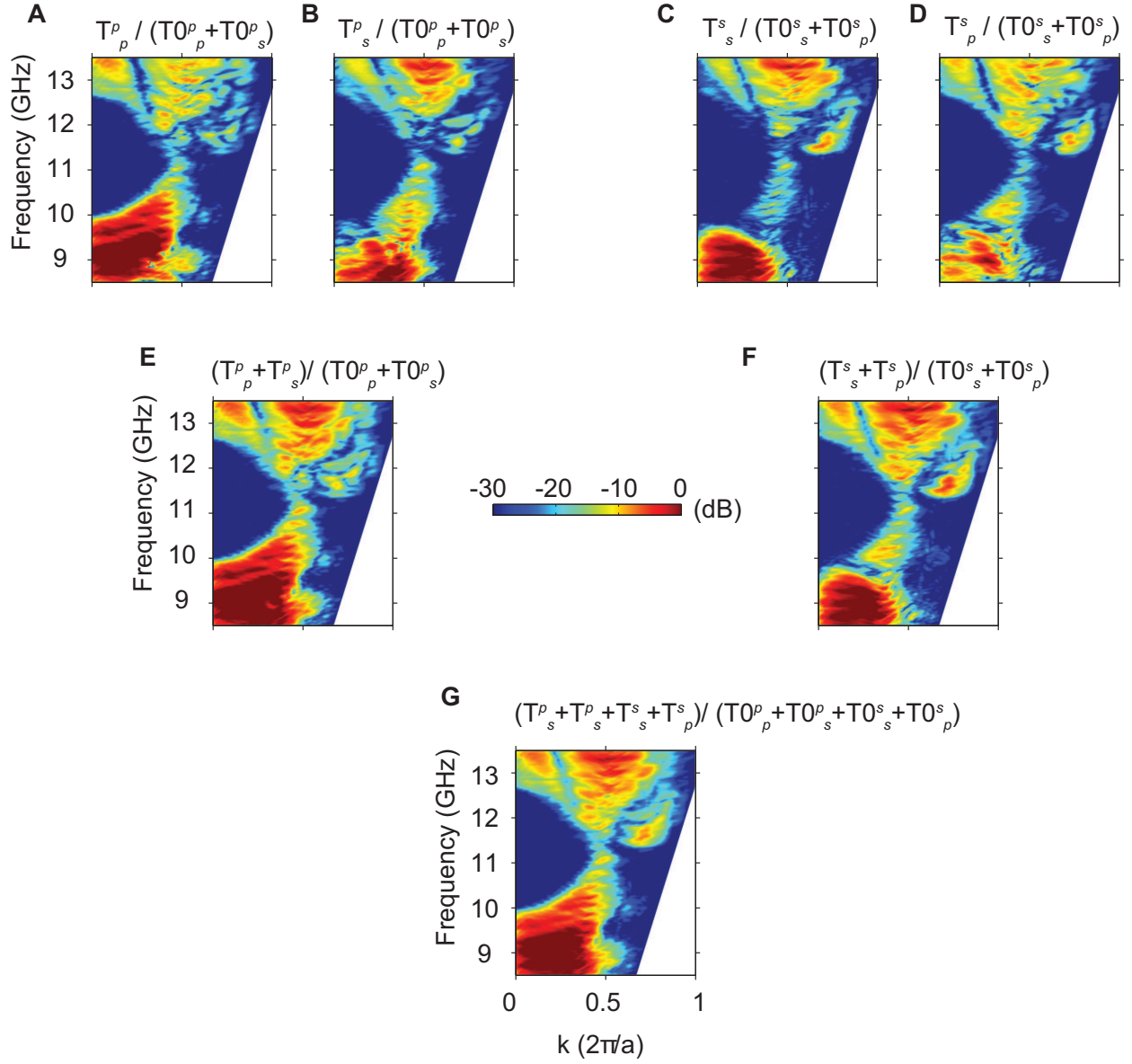


FIG. S2: Transmission power averaged over different polarization channels, when $\alpha = 90^\circ$.

$T_{\text{receiving-polarization}}^{\text{incident-polarization}}$ represents transmitted power through sample. $T0_{\text{receiving-polarization}}^{\text{incident-polarization}}$ represents transmitted power without the sample. (G) is the final data plotted in Fig. 3C.

$$\alpha = 0^\circ (\Gamma\text{-N})$$

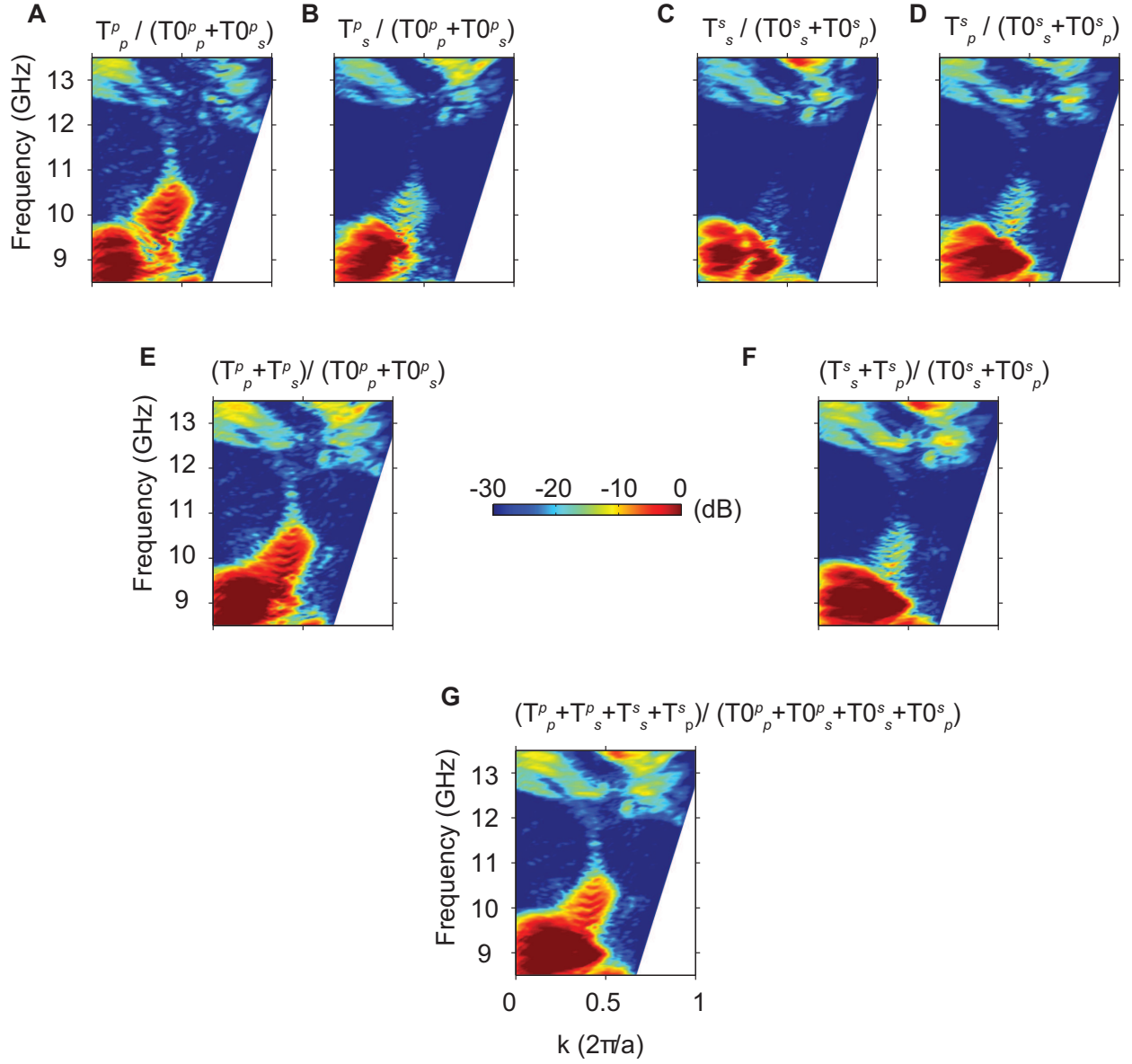


FIG. S3: Transmission power averaged over different polarization channels, when $\alpha = 0^\circ$.

$T_{\text{receiving-polarization}}^{\text{incident-polarization}}$ represents transmitted power through sample. $T0_{\text{receiving-polarization}}^{\text{incident-polarization}}$ represents transmitted power without the sample. (G) is the final data plotted in Fig. 3C.